Aerodynamics and Acoustics of Da Vinci Aerial Screws

Koushik Marepally†
Postdoctoral Research Associate

Ron Berlin†
Undergraduate Student

James Baeder†
Professor

†Alfred Gessow Rotorcraft Center, University of Maryland, College Park, MD, USA

ABSTRACT

This study investigates the aerodynamic and acoustic performance of aerial screws, a helical rotor concept first envisioned by Leonardo da Vinci. Using high-fidelity Computational Fluid Dynamics (CFD) and aeroacoustic simulations, we analyze a range of screw geometries to identify the flow structures and design parameters critical to thrust generation. A dominant mechanism—the formation of a coherent, shape-conforming "da Vinci vortex"—is shown to govern performance, enabling figures of merit up to 0.64 in optimized configurations. Parametric studies reveal that bilinear variations in pitch and taper significantly outperform linear designs by enhancing vortex anchoring and minimizing swirl-induced energy losses. Wake analyses confirm that early contraction and reduced radial dispersion are strong indicators of aerodynamic efficiency. Acoustic evaluations discovered a unique noise radiation pattern for the aerial screws, with perceived noise level similar to or lower than notional conventional rotors operating for same thrust output.

INTRODUCTION

The aerial screw, first conceptualized by Leonardo da Vinci in the late 15th century, represents one of the earliest recorded visions of vertical flight. Da Vinci's manuscripts, rich in mechanical sketches and anatomical studies, include a helical rotor intended to generate lift by "screwing" into the air—a concept inspired by observations of vortical motion in both natural and mechanical systems. Though never realized in physical form during his lifetime, the design —shown in Figure 1 — was emblematic of da Vinci's proto-scientific approach, combining empirical reasoning with imaginative engineering. Lacking the materials, propulsion technologies, and scientific framework to validate such a system, the concept remained theoretical for centuries. It was not until the late 1800s that early hardware attempts were made using high-solidity, screw-like rotors (Ref. 1), though these efforts were hindered by fabrication limitations and a lack of rigorous aerodynamic understanding (Ref. 2).

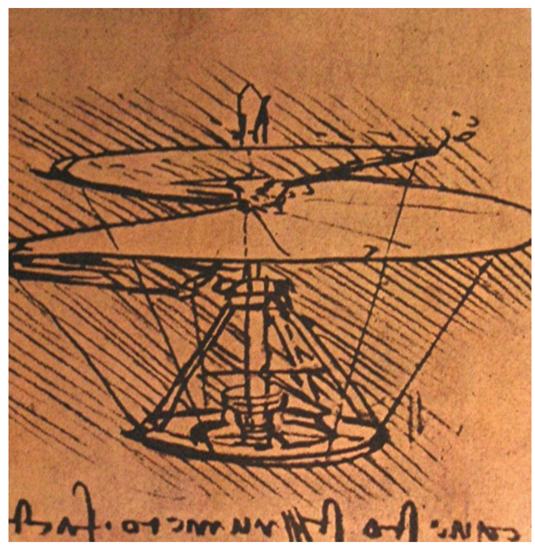

Figure 1. Leonardo's Aerial Screw Depicted in the Page of Paris Manuscript B, Folio 83v

As rotorcraft technology evolved in the 20th century, aerial screw concepts were largely displaced by more efficient rotor systems. The advent of thin, high-aspect-ratio blades and airfoil-based lift theory led to the dominance of conventional helicopter rotors, which offered higher aerodynamic efficiency, controllability, and structural simplicity. These systems, typically operating in the regime of blade element theory (BET) and momentum theory, became the backbone of practical vertical flight. In contrast, aerial screws remained without a coherent aerodynamic framework, and thus received little attention from the scientific community.

A resurgence of interest in helical rotor systems was triggered by the Vertical Flight Society's 2020 Annual Design Competition (Ref. 3), which encouraged unconventional VTOL architectures. Leveraging modern tools such as high-fidelity CFD, additive manufacturing, and precise flow diagnostics, several research groups revisited the aerial screw concept (Refs. 4,5).

These studies revealed that such rotors are capable of producing meaningful thrust with surprisingly competitive efficiency for hovering conditions—reporting figures of merit (FM) as high as 0.52—and are particularly well-suited for compact UAV and VTOL applications (Refs. 6, 7).

Crucially, the thrust generation mechanism in aerial screws deviates from conventional rotorcraft theory. Rather than relying on distributed lift from classical airfoil sections, the aerial screw operates via the formation of a coherent helical vortex structure, often termed the *da Vinci vortex* (Refs. 4, 8–10), as seen in Figure 2. This vortex conforms to the screw's geometry and induces localized low-pressure regions on the blade surface, producing net upward force. The flow physics is analogous to vortex-lift mechanisms observed in delta wings and highly swept planforms operating at high angles of attack (Ref. 11).

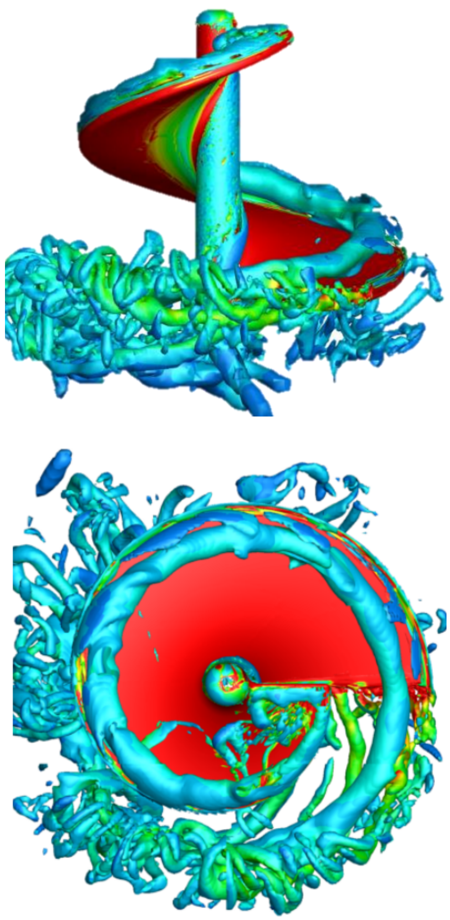

Figure 2. Iso-surfaces of vorticity Q-criterion around a Notional Hovering Aerial Screw: Top: Side View; Bottom: Top View)

CFD simulations show that the vortex originates near the leading edge, where three-dimensional separation and roll-up begin. As the blade rotates, the vortex migrates outward and wraps around the screw, forming a shape-conforming, helical structure that governs the pressure field. Tapered blade geometry plays a key role in maintaining vortex coherence by promoting spanwise pressure gradients and vorticity accumulation. As in delta wing aerodynamics, this taper-induced vortex strengthening enhances suction and improves thrust production.

Importantly, the thrust contribution is concentrated in the outboard regions of the blade, where the *da Vinci vortex* is strongest. The inboard sections, closer to the hub, experience weaker flow structures and lower pressure differentials, contributing minimally to net thrust. This non-uniform loading profile suggests that geometric optimization—particularly in the outer blade span—is central to improving performance.

Building on these foundations, the present study investigates the aerodynamics and acoustics of aerial screws, with emphasis on the role of blade geometry (pitch, taper) in influencing the *da Vinci vortex* and resulting thrust generation. The authors also use the CFD predictions to investigate the wake dynamics, induced velocity distributions, and noise radiation patterns. Performance metrics are compared with those of conventional rotors to assess the feasibility of aerial screws in next-generation vertical lift applications.

INFLUENCE OF AERIAL SCREW DESIGN ON THE AERODYNAMICS

The aerodynamic performance of aerial screws is fundamentally governed by the interaction between surface geometry and the flow-induced vortex structures. Among the most influential geometric parameters are the pitch rate and taper rate, both of which directly modulate the strength, coherence, and orientation of the pressure forces responsible for thrust generation. This section presents a systematic exploration of how pitch and taper, both in linear and bilinear configurations, affect the hover performance of aerial screws. The Figure of Merit (FM) is used as the primary performance metric, normalized for a constant thrust requirement.

Effect of Pitch Rate

The pitch rate ζ defines the axial advancement per revolution and directly controls the inclination of the screw surface relative to the axis of rotation. An increase in ζ leads to a steeper surface orientation, which reduces the axial projection of pressure-induced normal forces, thereby altering the net thrust-to-torque balance.

To understand the effect of pitch rate, several screws with a constant taper rate $\eta = 0.5$ and $R_{\text{max}} = 1$ ft are studied, with each screw having a different uniform pitch rate. The tip Mach number at the trailing edge is maintained at 0.25 for all these screw designs, which corresponds to a tip Reynolds number of 1.7×10^6.

Figure 3 shows the variation of FM with varying pitch rates. At low pitch rates (e.g., $\zeta = 1$), the surface is more aligned with the vertical axis, ensuring that a larger portion of the pressure loading contributes directly to thrust. As ζ increases to a moderate value (e.g., $\zeta = 1.2$), the aerodynamic efficiency improves due to enhanced vortex strength and an improved

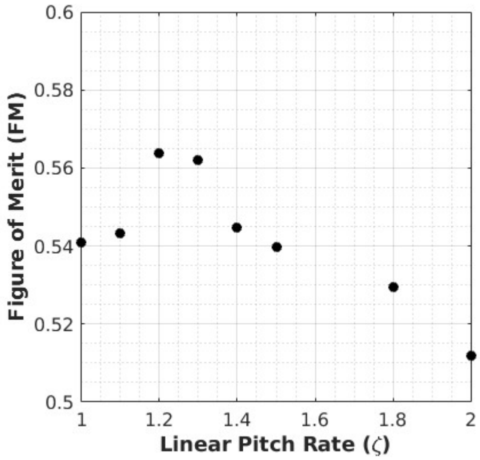

Figure 3. Variation of Figure of Merit for Screws with Different Linear Pitch Rate and Constant Linear Taper Rate ($\eta = 0.5$)

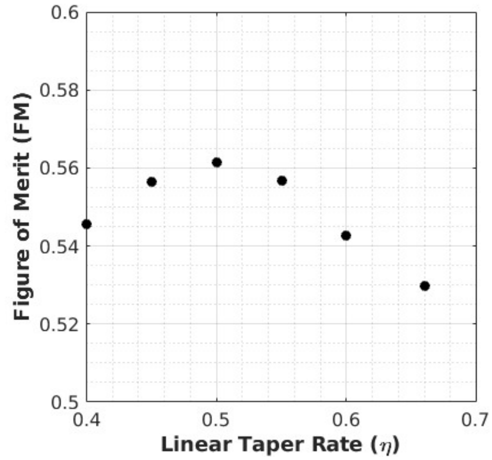

Figure 4. Variation of Figure of Merit for Screws with Different Linear Taper Rate and Constant Linear Pitch Rate ($\zeta = 1.2$)

balance between suction and surface orientation. This leads to a peak in FM, as the beneficial effects of increased vortex-induced suction outweigh the penalties in axial projection.

However, further increases in pitch (e.g., $\zeta = 1.5$) result in diminishing returns. Although the pressure differential ΔC_P continues to grow due to stronger leading-edge separation and tip vortex formation, the component of this force aligned with the thrust direction drops significantly. This leads to higher torque requirements and reduced FM, despite larger absolute normal forces. The shift in force orientation becomes the limiting factor in performance at high pitch rates.

To explore non-uniform pitch strategies, bilinear pitch distributions were investigated. These designs applied a lower pitch rate in the upstream (leading-edge) region followed by a higher pitch in the downstream half, while preserving the same mean pitch. This azimuthal shaping better aligns the leading-edge surface with the incoming flow, promoting early vortex formation and efficient axial loading. A modest ($\sim$1%) improvement in FM was observed compared to uniformly pitched screws, confirming the utility of azimuthally tailored pitch profiles.

Effect of Taper Rate

Tapering defines the radial contraction of the screw surface along the azimuthal direction. It modulates the local aspect ratio, flow acceleration, and spanwise pressure gradient — key drivers of vortex growth and coherence.

Similar to the effect of pitch rate, the effect of taper rate on the performance of the screw is studied by comparing the screws with all other design variables unaltered. Several screws with a constant pitch rate $\zeta = 1.2$ and $R_{\text{max}} = 1$ ft are studied, with each screw having a different uniform taper rate. The tip Mach number and the tip Reynolds number are maintained the same. Figure 4 shows the variation of FM for screws with varying taper rate.

In uniformly tapered screws, moderate taper rates (e.g., $\eta = 0.5$) tend to perform best. They reinforce the formation of a stable and coherent *da Vinci vortex*, which remains attached and concentrated across the blade span. However, as taper becomes more aggressive (e.g., $\eta > 0.6$), the effective lifting area is reduced, particularly near the trailing edge where thrust is most efficiently generated. Although the vortex structure remains coherent, the reduction in working surface area leads to a consistent drop in aerodynamic performance.

Interestingly, pressure load distributions indicate that aggressive taper reduces flow separation at the leading edge, particularly in low aspect ratio inboard sections. However, this benefit is not sufficient to offset the loss of spanwise thrust-producing area.

To balance vortex reinforcement and lifting area, bilinear taper profiles were studied. These designs applied aggressive tapering in the first half of the screw to promote strong vortex initiation, followed by an untapered or mildly tapered second half to retain effective area for pressure loading. These profiles led to a notable increase in FM—up to 5% improvement over the best-performing linearly tapered designs. This result emphasizes the critical role of front-loading the vortex formation, while retaining lifting surface in the regions where axial projection is most favorable.

Combined Variation of Pitch and Taper

A final design variant combined both optimal pitch and taper bilinear strategies: a modest initial pitch paired with aggressive early taper, followed by complementary downstream values. This configuration achieved a peak FM of 0.64, representing a 13% improvement over linear designs and 8% over the best bilinear single-variable cases.

These results underline a key principle in aerial screw design: the shape and timing of azimuthal flow–structure interaction are more influential than uniform parameter tuning. By tailoring pitch and taper profiles to optimize vortex initiation and axial force alignment, it is possible to significantly enhance aerodynamic efficiency, even in highly unconventional rotor systems like aerial screws.

COMPARISON OF AERIAL SCREW PERFORMANCE WITH CONVENTIONAL ROTORS

Geometry of Aerial Screws

The best performing screw designs from linear and bilinear combinations of screw pitch and taper are considered for comparison with a conventional rotor, for both aerodynamic performance and aeroacoustic signature. The geometric distribution of the pitch and taper rates (ζ_1, ζ_2, η_1, η_2) corresponding to the first and second half of the screw surfaces for each of these geometries are in Table 1

ID	Description	ζ_1	ζ_2	η_1	η_2
S1	Linear pitch and taper	1.2	1.2	0.5	0.5
S2	Bilinear pitch	1.0	1.4	0.5	0.5
S3	Bilinear taper	1.2	1.2	0.8	0.0
S4	Bilinear pitch and taper	1.0	1.4	0.8	0.0

Table 1. Different Aerial Screw Geometry Definitions

Computational Fluid Dynamics (CFD) is used for the aerodynamic analysis of the flow around these hovering screws using HAMSTR (Ref. 12), UMD's in-house CFD solution framework. HAMSTR employs Hamiltonian paths and strand grids based solution methodology, coupled with overset meshes for farfield computations. DDES (Delayed Detached Eddy Simulation) is the mathematical model used to describe the flow, with SA (Spalart-Allmaras) turbulence closure model, and fully turbulent flow assumptions.

The comparison is made at a constant dimensional thrust generated by each of these rotors, which is chosen to match that of screw S1 (best linearly pitched and tapered screw), operating at a tip Mach number of 0.25. The size of all the screws is maintained the same as 1 ft in radius ($R_{\max}$), and the RPMs of the screws S2, S3 and S4 are adjusted to achieve the same target thrust. Table 2 shows the operating tip Mach numbers of the different screws and their corresponding figures of merit.

Figure 5 shows the normal pressure load coefficient (difference between surface pressures across the top and bottom surface) for screws S1, S2, S3 and S4. Compared to S1, S2 has a lower pitch rate near the leading edge region, resulting in a weaker *da Vinci vortex*. However, this region has smaller axial contributions and larger torque-wise contributions, which favors low power characteristics of S2. The loss in thrust is compensated by the second half region of the screw with aggressive pitch rate.

For the screw S3, the second half region of the screw is untapered, resulting in less strengthening of the *da Vinci vortex* in this region. This is compensated by an aggressive taper in the first half compared to S1, resulting in improved performance. Screw S4 combines both the variations in pitch and

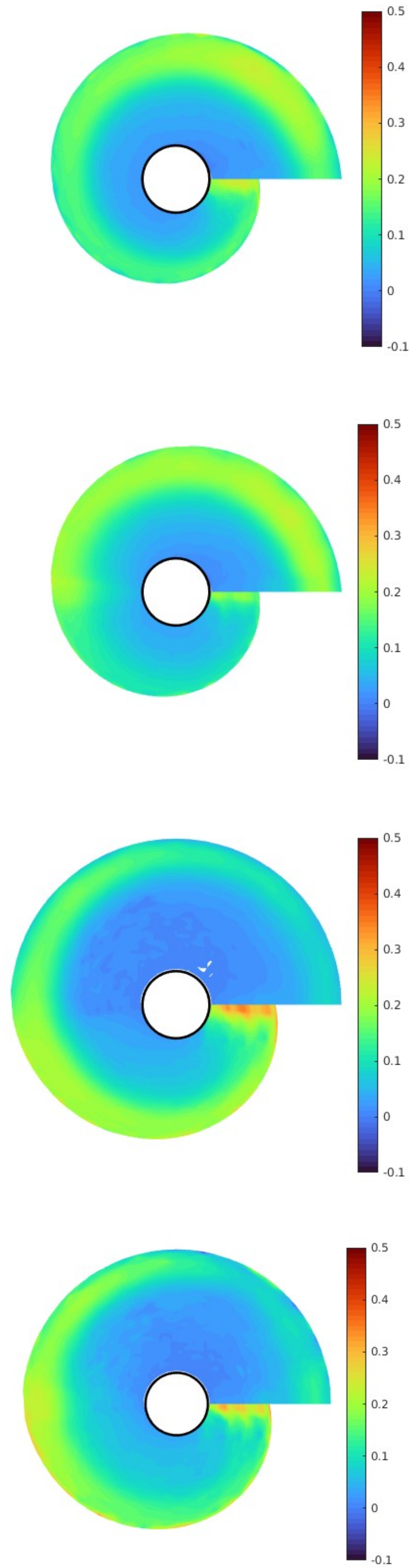

Figure 5. Surface Pressure Difference (ΔC_P) across Top and Bottom Surfaces for Screws S1, S2, S3 and S4

ID	Description	Tip Speed ($M_{tip}/M_{tip,S1}$)	Rotor Size ($R_{max}/R_{max,S1}$)	FM
S1	Screw 1 (Linear Pitch and Linear Taper)	1.000	1.000	0.561
S2	Screw 2 (Bilinear Pitch and Linear Taper)	0.981	1.000	0.567
S3	Screw 3 (Linear Pitch and Bilinear Taper)	0.937	1.000	0.591
S4	Screw 4 (Bilinear Pitch and Bilinear Taper)	0.878	1.000	0.640
C2.1	Conventional Rotor (2 blades, Size matched)	1.240	1.000	0.726
C2.2	Conventional Rotor (2 blades, Tip Speed matched)	1.000	1.240	0.731
C4.1	Conventional Rotor (4 blades, Size matched)	1.160	1.000	0.769
C4.2	Conventional Rotor (4 blades, Tip Speed matched)	1.000	1.160	0.771

Table 2. Comparison of the Operating Speeds, Rotor Sizes and Figures of Merit for Different Aerial Screws and Conventional Rotors

taper profiles, resulting in a much favorable load distribution and improved performance.

Geometry of the Conventional Rotor

For comparison, two notional conventional rotors are designed, one with 2 blades and the other with 4 blades. Both rotors have rectangular planforms, with a uniform twist rate of 20° from root to tip, and Clark-Y airfoil throughout the cross section. The choice of the airfoil is made based on the operating Reynolds number. The collective of the blade is adjusted to achieve an optimal figure of merit. The solidity of each of the rotors is maintained at 0.16.

Since the aerial screws are of extremely high solidity, conventional rotors can not achieve the same thrust at same size and tip speed. Two versions of the conventional rotors are investigated, viz., one with same rotor size but trimmed with RPM and the other with same tip speed but of a larger size.

Table 2 shows the operating conditions for the different rotors at matched thrust, and a comparison of the figures of merit for these conditions. The tip speed and rotor size are given relative to Screw 1, and the FM is absolute.

All the conventional rotors we observed to achieve a higher FM compared to aerial screws. Among the conventional ones, the rotors with 4 blades show better performance than those with 2 blades. Also, the larger rotors at smaller RPMs have slightly better performance than smaller rotors with higher tip speeds.

INVESTIGATION OF ROTOR WAKE AND INDUCED VELOCITIES

The best performing screw designs (S1, S2, S3 and S4) are investigated to understand the effect of vortex-based thrust on the induced velocity and wake behavior. Since the thrust generation is distributed across the length of the aerial screw, the wake behavior is different from the conventional rotor and understanding the induced velocity and wake contraction becomes important to further improve the screw performance.

Azimuthal averaged velocity fields are investigated on planes parallel to the rotor plane, at different axial locations below the screw, viz., 5%, 25%, 50% and 100% R_{max} from the trailing edge of the rotor blades. Figure 6 displays the variation of axial, radial and tangential components of the averaged velocities with radial distance, for screw S1. The velocities are normalized with rotor tip speed, and the radial distances with rotor radius.

It is observed that the wake contracts from 5% R_{max} to 50% R_{max}, and then expands beyond. This is a non-ideal contraction of the wake, which is an indication of loss of flow energy to swirl or radial components and thereby lowering the figure of merit.

Radial velocity plot displays inward velocity profiles for wake-ages upto 50% R_{max}, indicating desirable wake contraction trends. At 100% R_{max} station, the profile is radially outward, indicating a wake expansion in the region. The swirl velocity remains similar along the axis, and is significant in the inboard regions.

Figure 7 shows the instantaneous snapshot of wake profiles 50% R_{max} below the trailing edge, for screw S4. The coordinate axes are normalized with rotor radius and the wake velocities with rotor tip speed. The axial velocity profile shows nearly uniform downwash region, with a small instantaneous upwash region corresponding to the local vortex induced flow.

Figure 8 shows the comparison of azimuthal averaged wake profiles for different screws. All the screws display a similar wake geometry, with screw S4 showing a complete wake contraction by the axial station 50% R_{max}. The interior region of the wake is more uniform for the screw S4, as indicated by a flat radial velocity profile with minor contraction zone in the outboard region. This indicates more ideal wake contraction, as is observed in the high FM of S4. Screws S1, S2 and S3 require larger wake-age to achieve complete contraction, indicating higher losses of axial momentum to swirl.

The wake analysis in this study provides valuable insights that translate directly into aerial screw design strategies. Among the configurations studied, the bilinear pitch and taper screw exhibited the most desirable wake characteristics, with complete contraction observed within 50% R_{max} below the rotor. This early and coherent wake contraction is indicative of efficient momentum transfer and reduced energy loss to non-thrust-contributing components such as swirl and radial

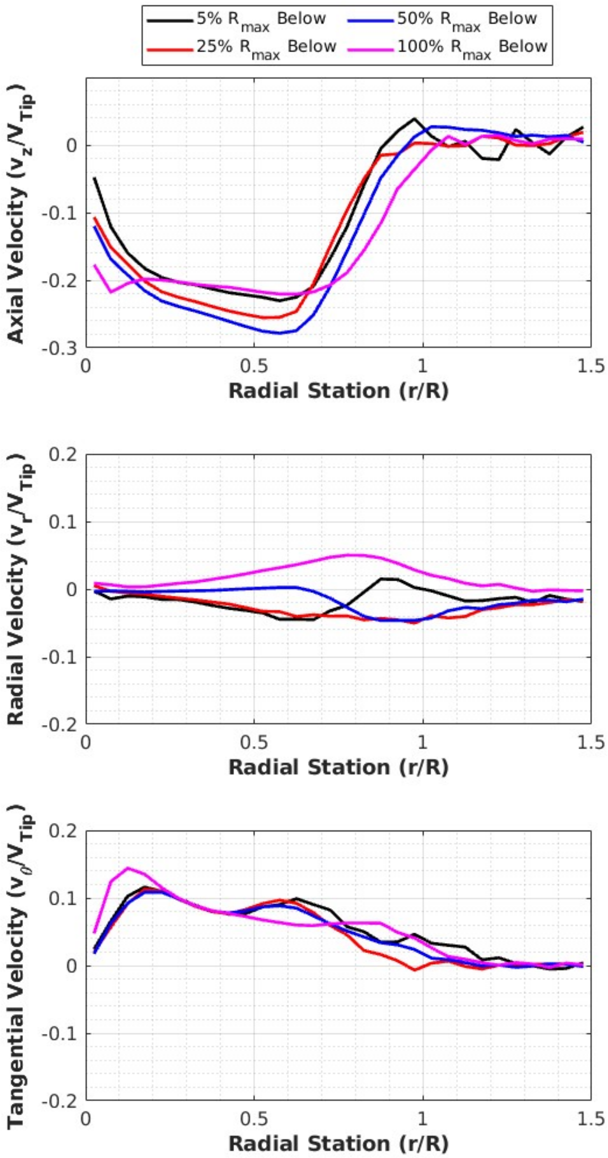

Figure 6. Azimuthal Average Wake Velocity Profiles for the Screw S1: Top: Axial Velocity; Middle: Radial Velocity; Bottom: Swirl Velocity

outflow. In contrast, linearly pitched and tapered screws exhibited slower contraction and more diffused wake structures, corresponding to a measurable drop in figure of merit. These observations suggest that carefully tuning the azimuthal variation of pitch and taper is critical for optimizing the screw's aerodynamic performance. An aggressive initial taper promotes early *da Vinci vortex* formation, strengthening thrust generation, while a more gradual taper downstream supports sustained vortex coherence. Similarly, a bilinear pitch profile can improve the projection of surface pressure forces in the axial direction, thereby minimizing swirl-induced losses. The wake profile, therefore, serves not merely as a diagnostic outcome but as a key design tool—enabling identification

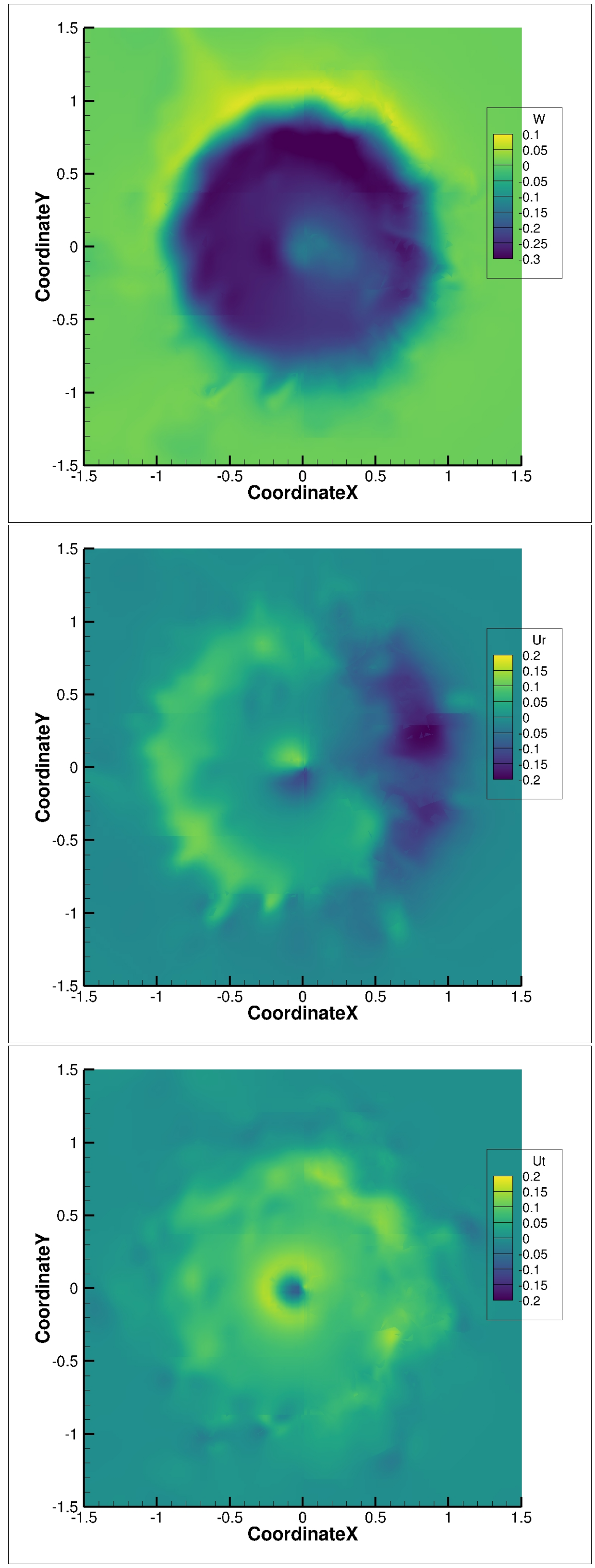

Figure 7. Instantaneous Wake Velocity Profiles for Screw S4 at an Axial Loation 50% Below Trailing Edge: Top: Axial Velocity; Middle: Radial Velocity; Bottom: Swirl Velocity

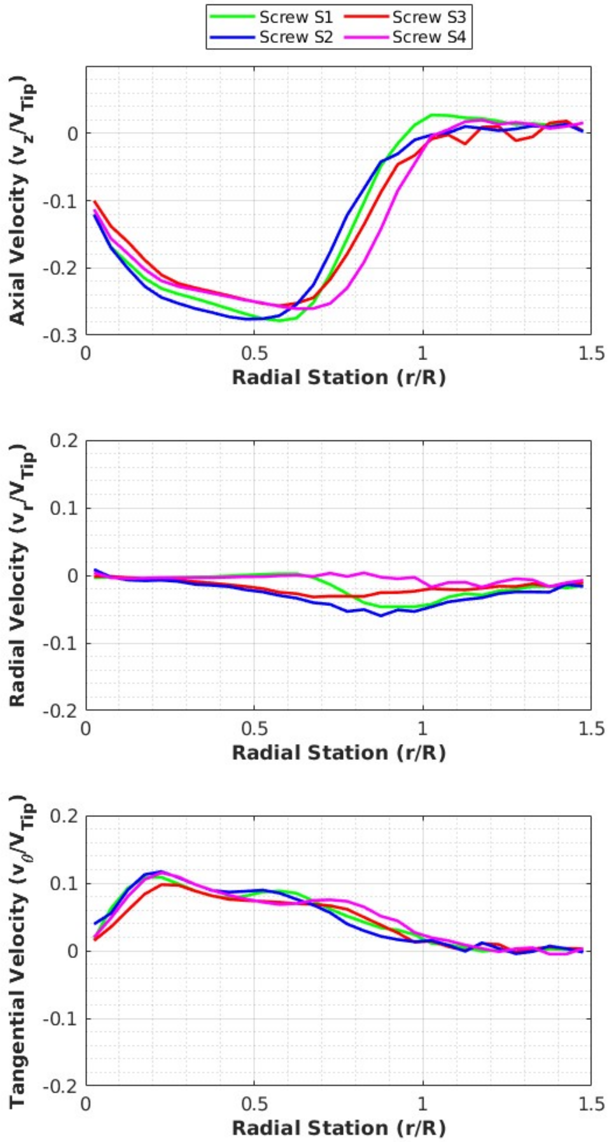

Figure 8. Azimuthal Average Wake Velocity Profiles for Different Screws at 50% R_{max} Axial Station: Top: Axial Velocity; Middle: Radial Velocity; Bottom: Swirl Velocity

of flow behaviors that directly impact efficiency. By targeting early vortex anchoring, reducing swirl, and promoting inward radial flow near the root, future aerial screw designs can be better tailored to exploit the vortex-based thrust mechanism central to their operation.

AEROACOUSTIC ANALYSIS OF DA VINCI SCREWS

The aeroacoustic analysis of the screws is performed using ACUM (Ref. 13), the University of Maryland's in-house acoustic prediction toolchain. ACUM utilizes geometric and aerodynamic data from CFD simulations to compute thickness and loading noise components and predict sound pressure levels (SPL) at specified observer locations. The underlying computational framework is based on Farassat's Formulation 1A (Ref. 14) of the Ffowcs Williams–Hawkings (FW-H) equation (Ref. 15), which models both the thickness and loading contributions to tonal noise.

The acoustic signatures of various screw designs (S1, S2, S3, and S4) are compared against those of conventional rotors (C2.1, C2.2, C4.1, and C4.2). Observers are placed along a circular arc in a plane perpendicular to the rotor axis at a radial distance of 5 meters from the rotor center. For screws S1–S4 and rotors C2.1 and C4.1, this corresponds to approximately 16.5 rotor radii (R). Due to the larger diameters of C2.2 and C4.2, this observer distance represents a slightly smaller non-dimensional value for these rotors.

In this study, only the thickness and loading noise components are modeled using the FW-H formulation within ACUM. The self-noise components, typically modeled empirically, are excluded due to the lack of validated models for the unconventional screw geometries. For consistency, self-noise is also excluded from the conventional rotor predictions.

The input to the acoustic solver is derived from DDES simulations (using HAMSTR), which provide both the steady blade loading and unsteady pressure fluctuations associated with blade–wake interaction (BWI). These components are used to compute the acoustic signature of each rotor configuration. For the aerial screws, the aerodynamic simulation is resolved every 0.5° for one full rotor revolution. For the conventional rotors with N_b blades, the flow solution is resolved every 0.5° for $1/N_b$ rotor revolutions. The aerodynamics data is replicated for a full rotor revolution using a periodic assumption with period $1/N_b$.

Thickness Noise

Figure 9 shows the variation of the thickness noise acoustic pressure for different observer locations on the circle, for all the rotors.

The aerial screws, due to their distributed geometries, exhibit large thickness noise levels compared to conventional rotors. Similar to conventional rotors, the thickness noise due to aerial screws is dominant in-plane of the rotors and diminishes as the observer moves towards the rotor axis.

Conventional rotors operating at higher speed exhibited larger thickness noise levels compared to larger rotors at lower speeds. Also, the rotors with 4 blades have the least noise levels of all the conventional rotors and aerial screws.

Figure 10 shows the acoustic pressure waveforms at an observer located on the circle at 30° declination from the rotor plane. The peak-to-peak amplitudes of aerial screws are large compared to the conventional rotors, as predicted by the acoustic directivity chart. Due to the distributed geometry of the screws, the corresponding waveforms have a distributed frequency spectrum due to the interference pattern of axially distributed acoustic sources. Conventional rotors have dominant blade passage frequency components in the waveforms.

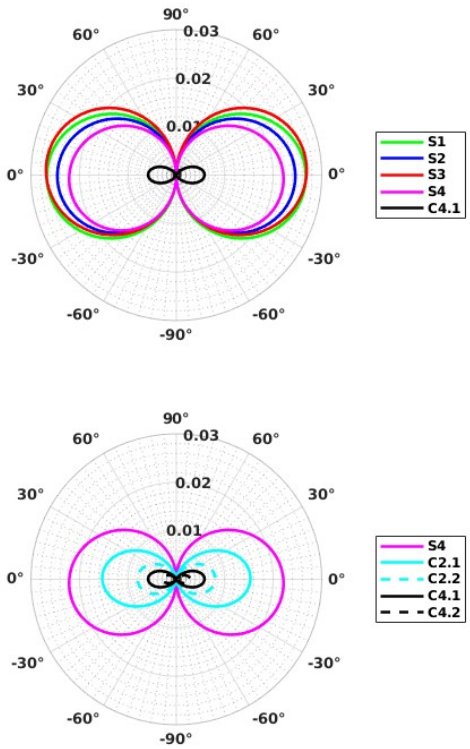

Figure 9. Directivity of Thickness Noise (p'_{rms} vs θ), Top: Screws S1, S2, S3 and S4 vs Conventional Rotor C4.1, Bottom: Screw S4 vs Conventional Rotors C2.1, C2.2, C4.1 and C4.2

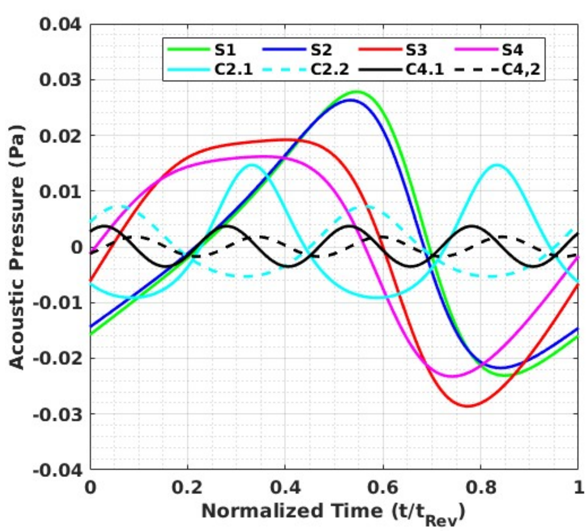

Figure 10. Thickness Noise Waveforms for Observer at $\theta = -30^\circ$ for different Rotors

Screws S1 and S2 have similar acoustic waveform, and S3 and S4 have a similar waveform, indicating that the thickness noise is more sensitive to screw taper distribution than pitch distribution.

While the noise levels of the conventional rotors are lower than the aerial screws, the corresponding blade passage tonal frequencies for screws are 1/Rev and for the conventional rotors are N_b/Rev. With the frequency adjustments for perceived loudness using A-weighting (Ref. 16), the perceived noise levels of aerial screws is lower than the conventional rotors.

Tonal Loading Noise (Steady Loads)

Figure 11 shows the variation of the acoustic pressure due to loading noise at different observer locations on the circle, for all the rotors. These estimates are based on the steady component of the loads (azimuthal invariants).

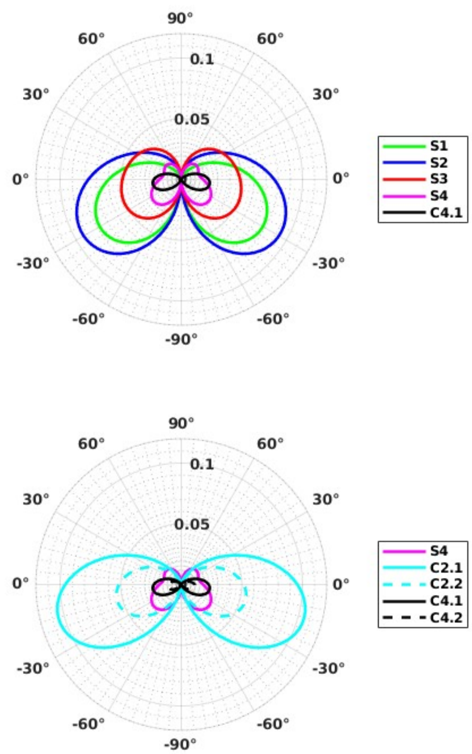

Figure 11. Directivity of Loading Noise due to Steady Loads (p'_{rms} vs θ), Top: Screws S1, S2, S3 and S4 vs Conventional Rotor C4.1, Bottom: Screw S4 vs Conventional Rotors C2.1, C2.2, C4.1 and C4.2

The loading noise levels are higher below the rotor plane compared to above, and diminish as the observer moves towards the rotor axis.

Conventional rotors with 2 blades exhibited the highest loading noise levels compared to all other rotors. Rotor C4.1 and screw S4 show similar noise levels, lower than the other screw geometries. All the screws show maximum noise at a declination of $\sim 30^\circ$ from the rotor plane, and conventional rotors show a maximum noise level at $\sim 15^\circ$.

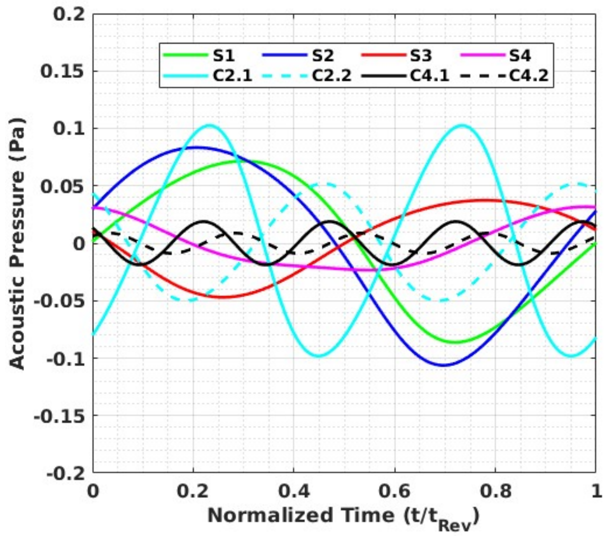

Figure 12. Loading Noise Waveforms (Steady Loads) for Observer at $\theta = -30°$ for different Rotors

Figure 12 shows the acoustic waveforms corresponding to steady loading noise at the observer located at 30° declination to the rotor plane. The peak-to-peak magnitudes of the conventional rotor with 2 blades are highest, followed by the screws S1 and S2. The waveforms corresponding to aerial screws contain higher harmonics of the rotor frequency, due to the distributed nature of acoustic sources.

Similar to the thickness noise, the perceived noise level is lower for the aerial screws for the steady loading component due to the differences in blade passing frequencies.

Loading Noise (Unsteady Loads)

DDES simulations are used to resolve larger turbulent structures in the flow, resulting in unsteady blade loads. These unsteady loads include the Blade-Wake interaction (BWI) component, resolved components of turbulence etc. These unsteady loads contribute to a broadband component of the loading noise. While the unsteady components are not periodic with rotor revolutions, the acoustic simulation is performed with the periodic assumptions. These assumptions result is minor inaccuracies to predict the acoustic content at non-multiples of the blade passage frequencies. However, major components of the broadband noise can be predicted using these unsteady loads.

Figure 13 shows the contours of root mean square (RMS) value of the fluctuations of surface pressure coefficient for the aerial screws S1, S2, S3 and S4, for upper and lower surfaces. These contours inform the locations of various acoustic sources corresponding to the unsteady loads on the rotors.

On the upper surface of the screw, the leading edge region contributes for the majority of unsteady aerodynamic loading, due to the presence of a LE vortex separation phenomenon. Also, the tip region around the *da Vinci vortex* also experiences unsteady pressures due to the unsteadiness of the vortex. The regions of pitch rate and taper rate transition in the screws S2, S3 and S4 are secondary zones of unsteadiness.

The lower surface of the screw contributes for the majority of unsteady loads for the aerial screws. These variations are larger towards the trailing edge of the screw, corresponding to the interaction of the screw surface with wake vorticity. The leading edge and tip region are secondary zones of unsteadiness, caused by the tip leakage of the vortices.

These unsteady loads contribute additional noise components that span a wide range of frequencies. For the aerial screws, the interaction with wake is a continuous event distributed along the rotor revolution. This results in a less impulsive noise signature.

However, for conventional rotors, of all the unsteady components, the BWI events are highly impulsive. These events occur when a blade passes the trailing wake due to the other blades. Due to smaller chord of the conventional rotors and large blade loadings, the duration of the interaction is small and the strength of the interaction is large, resulting in an impulsive load fluctuation.

In case of the rotors C2.x and C4.x, the solidity of the rotors remain the same, and thus C2.x rotors have a wider chord compared to C4.x. Thus, the BWI loads are relatively less impulsive for the rotors with two blades compared to those with 4 blades.

These unsteady loads are used in the noise computations, and the resulting noise directivity is shown in Figure 14. While the conventional rotors show a significant noise level in the axial direction, the aerial screws show a distinctive noise directivity concentrated towards $\sim \pm 15°$ from the rotor axis. The unsteady loading noise is smaller for the rotors C2.1 and C2.2, maintaining the directivity pattern of these rotors same as steady loads at angles away from the rotor axis. The directivity pattern of C4.1 and C4.2 is significantly changed to be dominant along the rotor axis due to high impulsive unsteady loads.

Figure 15 shows the comparison of loading noise waveforms received by observer located at 30° declination form the rotor plane, for the rotors S4, C2.1 and C4.1. With a unsteady acoustic sources distributed over the screw surface, the unsteady waveform of S4 has a wide range of overtones with diminishing magnitude superposed on the tonal waveform. Rotor C2.1 shows minimal deviation from the steady waveform, with a few distributed impulses due to BWI events. The unsteady waveform of C4.1 shows large and sharp fluctuations due to the impulsive BWI events. These sharp fluctuations contain a wide range of overtones of the blade passage frequency with large magnitudes.

Spectral decomposition of these waveforms is shown in Figure 16. While the unsteady loads produce a broadband noise signature, the impulsive unsteadiness of rotor C4.1 results in a high magnitude of the broadband spectrum. Due to the high frequency of the components of this noise, the perceived noise level of these components is very high, and is shown in the A-weighted noise spectrum in Figure 16. Figure 16 also compares the loading noise frequency spectrum to the tonal noise

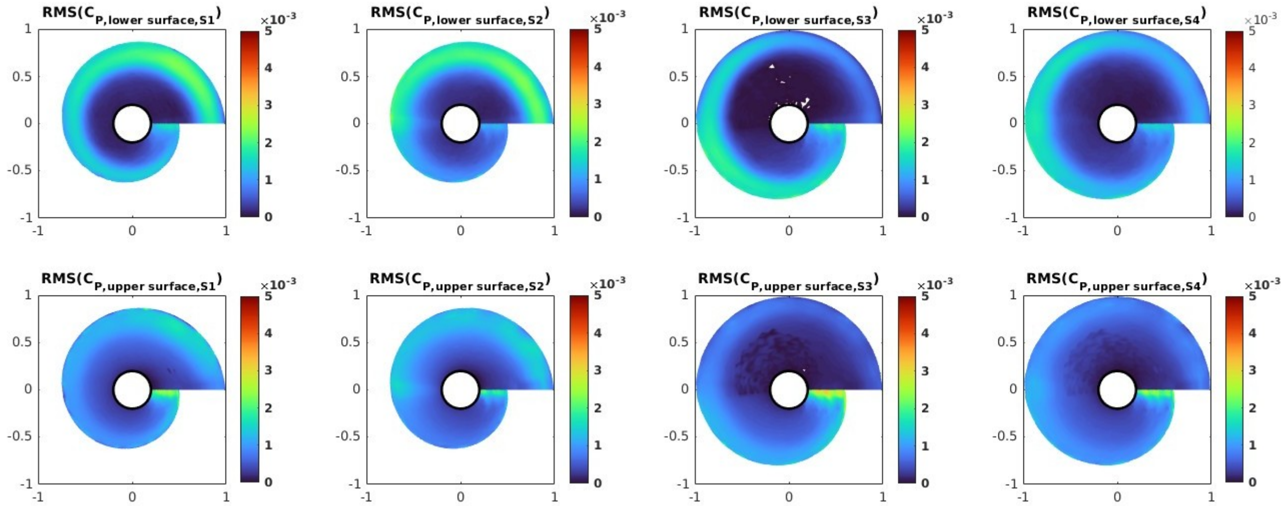

Figure 13. Contours of the RMS fluctuations of Surface Pressure Coefficient for Screws S1, S2, S3 and S4

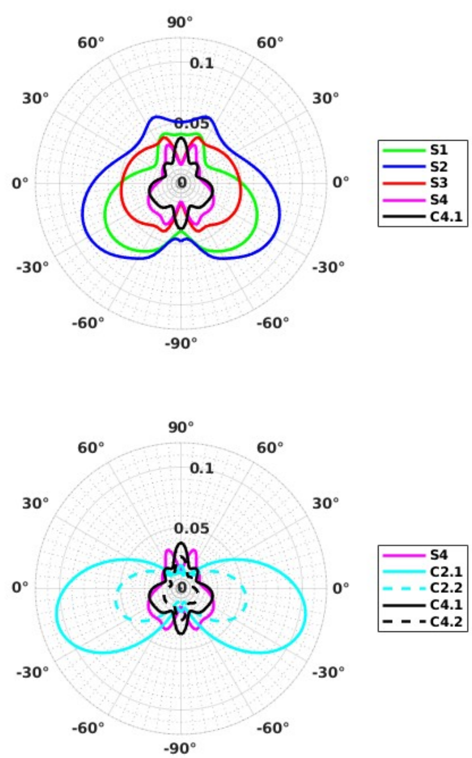

Figure 14. Directivity of Loading Noise due to Unsteady Loads (Steady and Blade Wake Interactions combined) (p'_{rms} vs θ), Top: Screws S1, S2, S3 and S4 vs Conventional Rotor C4.1, Bottom: Screw S4 vs Conventional Rotors C2.1, C2.2, C4.1 and C4.2

component due to steady loading. The amplitude of high frequencies is very low for the steady load noise, resulting in

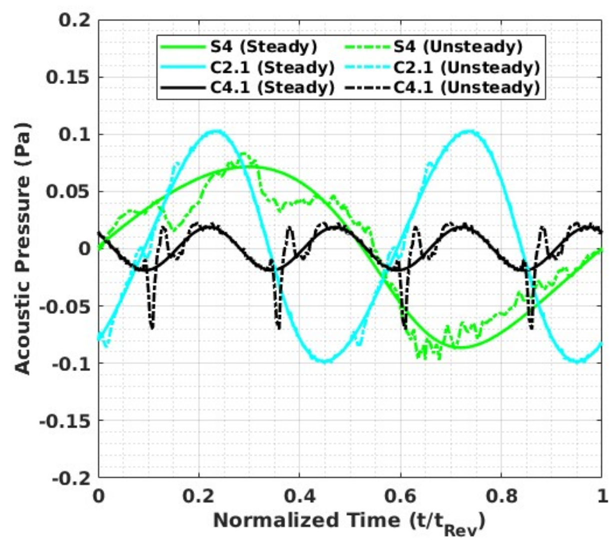

Figure 15. Loading Noise Waveforms (Steady vs Unsteady Loads) for Observer at $\theta = -30°$ for Rotors S1, C2.1 and C4.1

pure tones.

The effect of multiple blades, i.e., higher blade pass frequency is seen in the corresponding perceived noise level spectrum in Figure 16, where the tonal loading noise due to screw S4 is perceived ~ 30 dB less than the true amplitude, while that of C4.1 is only ~ 10 dB less.

Total Noise (Thickness and Loading)

All the noise components of thickness and loading are superposed to compute the total noise at each observer location for all the rotors.

Figure 17 shows the variation of sound pressure level at each observer location, expressed in dB scale. Overall noise level

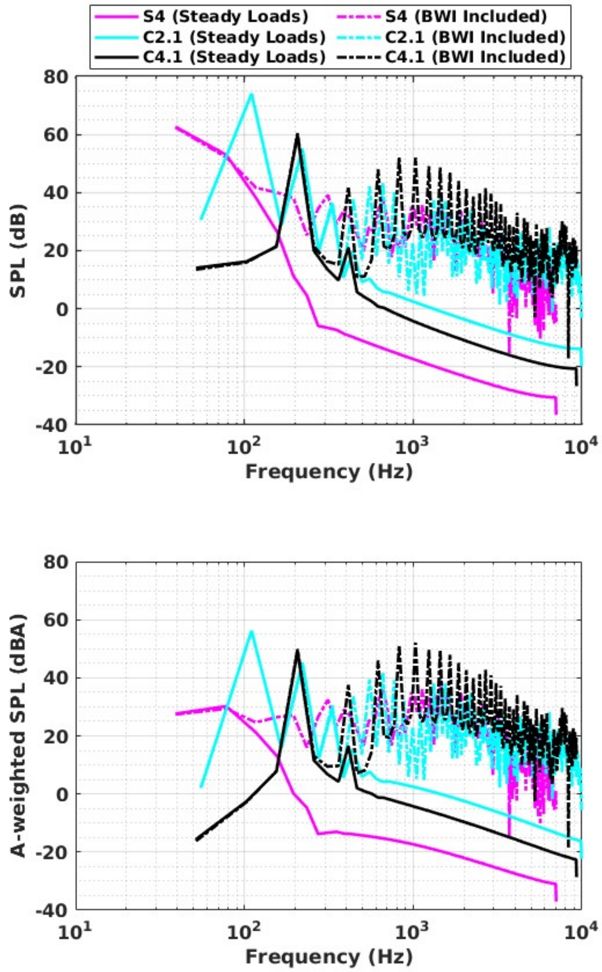

Figure 16. Spectral Decomposition of Loading Noise at Observer located at $\theta = -30°$ for Rotors S4, C2.1 and C4.1, Top - Sound Pressure Level (SPL) and Bottom - Perceived Noise Level (A-weighted SPL)

is low for the rotor C4.2 (except on the rotor axis). However, screw S4 has similar noise levels as rotors C4.x. The rotors with 2 blades have higher in-plane noise levels.

Figure 18 shows the variation perceived noise levels, using A-weighting. The tonal components of the aerial screws are significantly attenuated due to their low frequencies, resulting in a unique noise directivity pattern for all the screws. The noise level is low both in-plane and on axis, and is highest at $\sim 15°$ on either side of the rotor axis.

The noise directivity pattern of the conventional rotors shows a maximum on the rotor axis, due to high frequency content from broadband loading noise. With rotors C2.x having non-impulsive BWI loads, the noise directivity pattern is more in-plane.

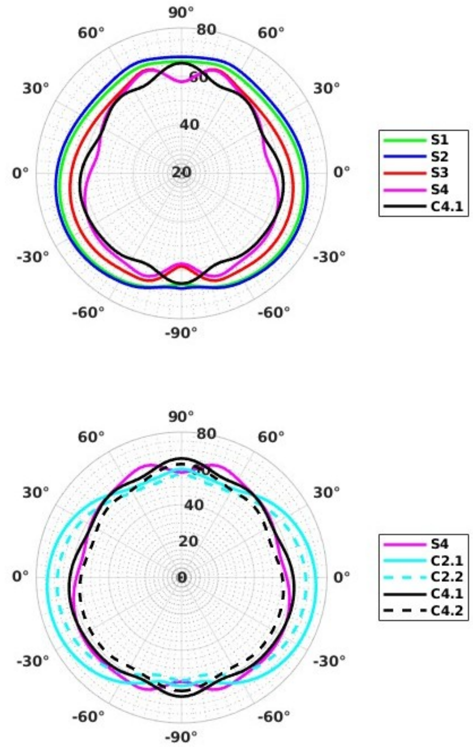

Figure 17. Total Noise Directivity for Different Rotors (SPL (dB))

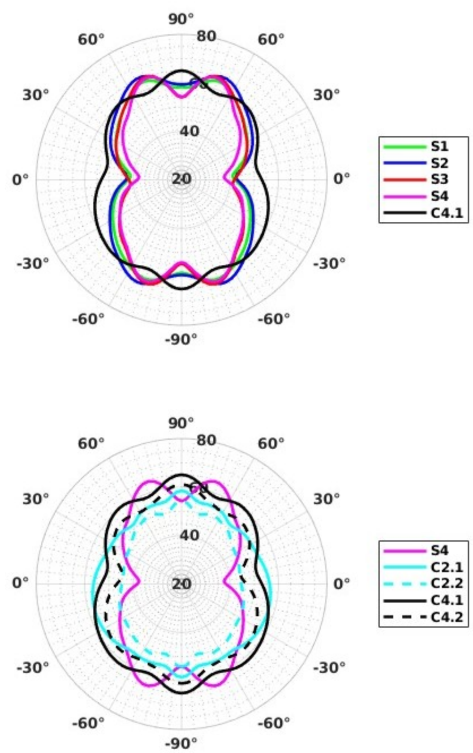

Figure 18. Total Perceived Noise Levels for Different Rotors (PNL (dBA))

CONCLUSIONS AND FUTURE WORK

This study presented a detailed investigation of the aerodynamic behavior of aerial screws, directly inspired by Leonardo da Vinci's early vision for vertical flight. A primary focus was placed on understanding the thrust generation mechanism governed by the "*da Vinci vortex*," a shape-conforming helical vortical structure that forms at the screw tip. Through Computational Fluid Dynamics (CFD) simulations, it was confirmed that this vortex plays a dominant role in establishing the pressure differentials necessary for thrust, functioning analogously to vortex lift observed in highly swept and delta wing configurations.

4 different screw geometries are studied on the aerodynamic performance and acoustics. Wake analyses provided crucial insights into the aerodynamic efficiency of different geometries. Efficient screws exhibited rapid and coherent wake contraction within 50% of the rotor radius downstream, minimized swirl velocity near the root, and maintained a stable downwash region. These flow features correlated directly with improved FM values and confirmed that the wake structure is not merely a byproduct of geometry but an active indicator—and driver—of aerodynamic efficiency. This positions wake behavior as a powerful diagnostic and design tool for future aerial screw development.

In addition to aerodynamics, this study performed a detailed acoustic evaluation using both tonal and broadband noise components derived from CFD. Aerial screws, due to their distributed surface and thick chord geometry, exhibited higher absolute thickness and loading noise compared to conventional rotors. However, their blade-passing frequencies occur at much lower harmonics (1/Rev), which results in significantly attenuated perceived loudness under A-weighted acoustic scaling. Furthermore, the broadband loading noise in aerial screws is less impulsive and more spectrally diffuse than in conventional rotors—particularly when compared to 4-blade systems where blade–wake interaction (BWI) creates sharp, high-frequency acoustic peaks. These differences suggest that aerial screws, despite higher raw acoustic power, may offer superior acoustic stealth in urban or low-speed VTOL environments.

When compared to notional conventional rotors, aerial screws were found to produce lower FM values (by about 10–20%), largely due to geometric inefficiencies and non-optimized flow structures. However, they also offer several offsetting advantages: (i) favorable perceived noise characteristics, (ii) simpler manufacturing of continuous helical geometries for low-speed applications, and (iii) opportunities for compact, high-thrust VTOL propulsion systems in size- or disk-constrained configurations.

Looking forward, several promising directions emerge for advancing the aerial screw from concept validation to practical deployment:

- Higher-order shaping strategies: Moving beyond bilinear profiles, future studies can investigate smoothly varying pitch and taper functions to finely tune local incidence angles and vortex anchoring locations. Optimization techniques or inverse design strategies can be employed to identify ideal geometries that maximize aerodynamic efficiency while minimizing torque penalties.
- Small-scale implementation: One of the most promising areas for aerial screw application lies in the micro-scale or nano-UAV regime, where conventional rotor aerodynamics break down due to low Reynolds number effects, increasing viscous losses, and reduced airfoil performance. Aerial screws, with their vortex-based thrust, are naturally suited to this regime. Their high solidity and shape-conforming vortex structures offer a viable alternative when traditional blade theory is no longer applicable. Investigating aerodynamic performance at scales ranging from a few centimeters to tens of centimeters will be an important next step, particularly for applications in indoor surveillance, swarm robotics, and autonomous inspection.

REFERENCES

1. Lambermont, P., and Pirie, A., *Helicopters and Autogyros of the World*, Barnes, 1970.
2. Baden-Powell, B., "Experiments with Aerial Screw Propellers," *Aeronautical journal (London, England: 1897)*, Vol. 8, (30), 1904, pp. 28–32. DOI: 10.1017/S2398187300142380.
3. Leonardo Helicopters, "37th Annual Student Design Competition - 2019-2020 Request for Proposal (RFP) - Leonardo's Aerial Screw: 500 Years Later," .
4. Sutherland, J., Brown, R., Ebewele, E., Fisler, E., Krohmaly, K., Linkins, J., Marepally, K., Prete, A., Semenov, I., Nagaraj, V., Chopra, I., and Datta, A., "Leonardo's Aerial Screw: 500 Years Later," University of Maryland, 2020.
5. Aşir, E., van Gaalen, K., van den Ham, M., Han, S., van Herwerden, T., Kerckhoffs, H., Kortenhorst, R., Pauly, N., Vleming, T., and de Voogt, R., "SolidityONE: Leonardo da Vinci's Aerial Screw," TU Delft, 2020.
6. Prete, A., Nagaraj, V., and Chopra, I., "Revolutionary Flight Vehicle Based on Leonardo da Vinci Aerial Screw: A Paradigm Shift in VTOL Technology," VFS Aeromechanics for Advanced Vertical Flight Technical Meeting, San Jose, CA, Jan 25-27, 2022, 2022.
7. Prete, A. C., *Revolutionary flight vehicle based on Leonardo Da Vinci Aerial Screw: a paradigm shift in VTOL Technology*, Master's thesis, University of Maryland, College Park, 2022.
8. Marepally, K., Berlin, R., and Baeder, J., "Details of Da Vinci Aerial Screw Physics, Aerodynamics and Performance," 50th European Rotorcraft Forum 2024, ERF 2024, Marseille, France, Sep 10-12, 2024, 2024.
9. Berlin, R., Marepally, K., and Baeder, J., "Improvements to the Da Vinci Aerial Screw as a VTOL Thrusting Alternative," 11th Biennial Autonomous VTOL Meeting and 12th Annual Electric VTOL Symposium, TVF 2025, Phoenix, AZ, USA, Feb 04-06, 2025, 2025.
10. Marepally, K., Berlin, R., and Baeder, J., "Exploration of Vortex-Thrust: Da Vinci Aerial Screw Physics, Aerodynamics and Performance," Vertical Flight Society 81th Annual Forum & Technology Display, VFS Forum 2025, Virginia Beach, VA, USA, May 20-22, 2025, 2025.

11. Polhamus, E. C., “A concept of the vortex lift of sharp-edge delta wings based on a leading-edge-suction analogy,” NASA TN D-3767, 1966.

12. Jung, Y. S., Govindarajan, B., and Baeder, J., “A Hamiltonian-Strand Approach for Aerodynamic Flows Using Overset and Hybrid Meshes,” VFS 72nd Annual Forum, West Palm Beach, Florida, 05 2016.

13. Amiraux, M., *Numerical simulation and validation of helicopter blade-vortex interaction using coupled CFD/CSD and three levels of aerodynamic modeling*, Ph.D. thesis, University of Maryland, College Park, January 2014.

14. Farassat, F., and Succi, G. P., “The prediction of helicopter rotor discrete frequency noise,” In: American Helicopter Society, January 1982.

15. Ffowcs Williams, J. E., Hawkings, D. L., and Lighthill, M. J., “Sound generation by turbulence and surfaces in arbitrary motion,” *Philosophical Transactions of the Royal Society of London. Series A, Mathematical and Physical Sciences*, Vol. 264, (1151), 1969, pp. 321–342. DOI: 10.1098/rsta.1969.0031.

16. Fastl, H., and Zwicker, E., *Psychoacoustics: Facts and Models*, Vol. 22, Springer Series in Information Sciences, Springer, third edition, 2007. DOI: 10.1007/978-3-540-68888-4.